INTERNATIONAL JOURNAL FOR NUMERICAL METHODS IN FLUIDS
Int. J. Numer. Meth. Fluids 2002; **39**:403–440 (DOI: 10.1002/fld.325)

Numerical simulation of fluid flows using an unstructured finite volume method with adaptive tri-tree grids

Z. Z. Hu, D. M. Greaves[‡] and G. X. Wu[*,†]

Department of Mechanical Engineering, University College London, Torrington Place, London, WCIE 7JE, U.K.

SUMMARY

A tri-tree grid generation procedure is developed together with a finite volume method on the unstructured grid for solving the Navier–Stokes equations. A hierarchic numbering system for the data structure is used. The grid is adapted by adding and removing cell elements dependent on the vorticity magnitude. A special treatment is developed to ensure good quality triangular elements around the cylinder boundary. The adopted finite volume method is based on the cell-centred scheme. The pressure–velocity coupling is treated using the SIMPLE algorithm. A modified QUICK scheme for unstructured grids is derived. The developed method is used to simulate the flow past a single and multiple cylinders at low Reynolds number. The obtained results are in good agreement with the published data. Copyright © 2002 John Wiley & Sons, Ltd.

KEY WORDS: unstructured hierarchical grid; tri-trees; adaptive remeshing; finite volume method; SIMPLE; separated flows and vortex shedding

1. INTRODUCTION

The first step in a numerical simulation of fluid flow is the creation of a suitable grid. For viscous and unsteady flow problems involving complex boundaries, it is desirable to use a grid generation algorithm that can automatically divide the fluid domain into elements. Wille [1] described two-dimensional triangular and three-dimensional tetrahedral grid generation using the tri-tree and the tetra-tree methods respectively. The hierarchical data structure of tri-tree and tetra-tree reference numbers allows the algorithm to perform both up- and down-searches in grid adaptation as required. Wille's tri-tree reference numbers are contained in a record consisting of nine integers in two-dimensional flow. The present work uses a reference numbering system developed by Samet [2, 3] originally for quad-tree grids, which enables the reference numbers to be stored as single integers. A special treatment is developed in the

[*] Correspondence to: G. X. Wu, Department of Mechanical Engineering, University College London, Torrington Place, London WCIE 7JE, U.K.
[†] E-mail: gx_wu@meng.ucl.ac.uk
[‡] Present address: Department of Architecture and Civil Engineering, University of Bath, Bath, BA2 7AY, U.K.

Received March 2001
Revised November 2001

present work to ensure good quality triangular elements around the cylinder boundary. Two steps are taken: the node stretching and the obtuse angle elimination.

Finite volume formulations involve discretization of the flow domain and then integration of the equations over each element. The method has most commonly been used on quadrilateral grids (for example, Patankar [4] and Franke *et al.* [5]). However, triangular grids are much more suitable for modelling curved and complex domain boundaries. There are only a limited number of papers in the literature which describe the finite volume method using triangular grids, because the discretized mathematical formulations are more complicated than for quadrilateral grids. For example, Pan and Cheng [6] considered the Euler equations on unstructured grids. Thomadakis and Leschziner [7] used a semi-staggered control volume for the momentum and pressure correction equations. More recently Chan and Anastasion [8] presented a cell-centre upwind scheme and solution based on the pseudo-compressibility technique. The present work is based on the cell-centred scheme with SIMPLE for the pressure velocity coupling. This is similar to the work by Davidson [9]. The major difference is that the formulation is used with the hierarchic and adaptive tri-tree grids developed in this paper. A modified QUICK scheme for non-uniform grids is also introduced. The test cases for a single and multiple circular cylinders at low Reynolds number show that the scheme is stable and the result is accurate.

2. THE TRI-TREE ALGORITHM

In tri-tree grids, the mesh generation starts from an equilateral triangle which encloses the fluid domain. A diagram of the tri-tree structure is shown in Figure 1. An initial equilateral triangle is divided into four new equilateral triangles. Each of these triangles is then divided into another four equilateral triangles, and so on.

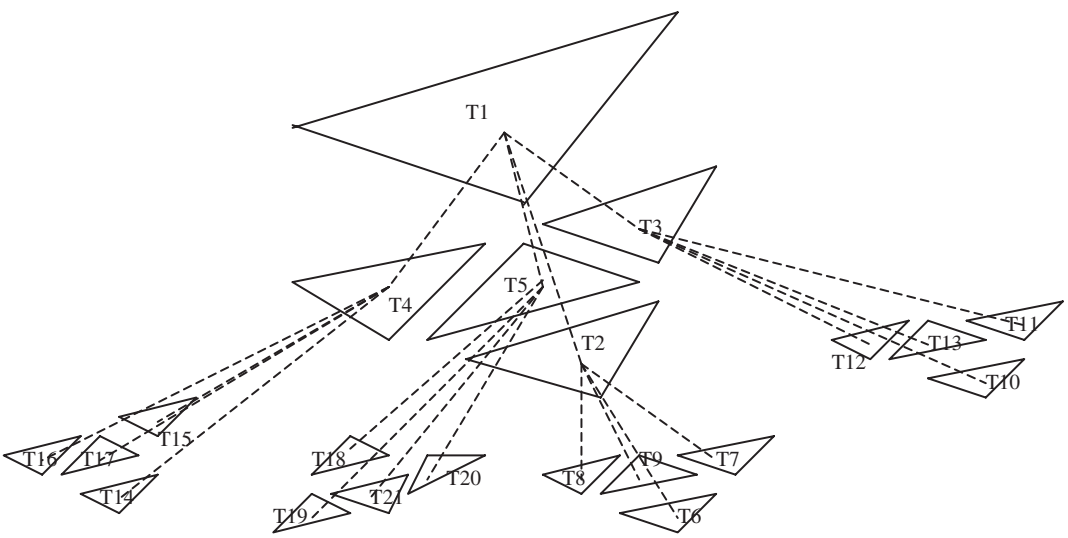

Figure 1. Tri-tree structure showing subsequent divisions.

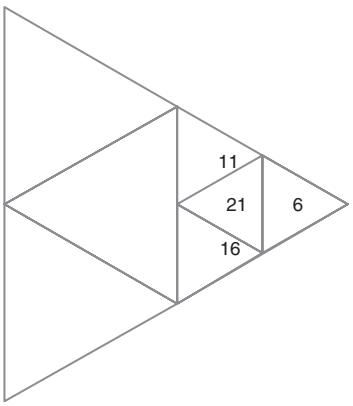

Figure 2. The reference numbers.

2.1. The numbering system

Each element has a reference number that indicates the position of the element within the tri-tree hierarchical data structure. The reference number is defined when the corresponding element is generated. It contains important information about the element. For example, the generation level, NL, and the reference numbers of parent and children elements of the present element, may be calculated directly from its reference number. The reference number can also be used to calculate its neighbour elements and to perform tree searches.

The reference numbering system for this study is adopted from Samet [2, 3], who stored the reference numbers efficiently as an integer. It can be summarized as

$$N = \sum_{i=0}^{m-1} N_i K^i \tag{1}$$

where m is the division level of the grid and N_i takes the integer value 1, 2, 3, or 4 depending on the position in which the element is located within its parent triangle. The tri-tree grid reference numbers are stored as the sum of successive powers of K. In this case, $K=5$ is used for tri-tree decimal grids in two dimensions. Within each divided element, the triangles are numbered anti-clockwise finishing with the central triangle (e.g. 21 in Figure 2).

The number of divisions required starting from the root element is the generation level of the element. Following from Equation (1) with $K=5$, the generation level is obtained by successively dividing the reference number by 5 until the remaining number is less than 1. For example, in Figure 3 the reference number of the element marked $*$ is 121. Successive divisions by 5 yield: first division $=24.2$, second division $=4.84$ and third division $=0.968$ which is less than 1 and so the operation is halted. Thus three divisions were carried out to produce a number less than one, which indicates that the generation level, $NL=3$.

To obtain the reference number of the parent element of a given triangle is a two-stage process. Firstly, the integer remainder of the division of the given element reference number by 5^{NL-1} is obtained. This is then multiplied by 5^{NL-1}. The procedure is

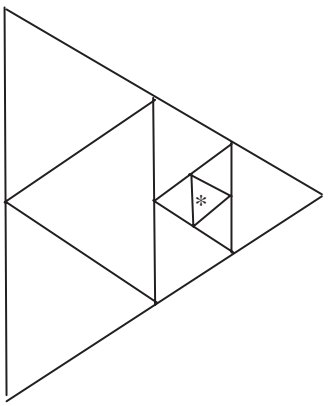

Figure 3. Example of tri-tree grid.

summarized by,

$$N_p = \mathrm{mod}\left(\frac{N}{5^{NL-1}}\right) \times 5^{NL-1} \tag{2}$$

where N_p is the reference number of the parent of a given element, mod is the integer remainder operator, and N is the given element reference number. For example, in Figure 3, the reference number of the element marked $*$ is 121; the generation level is 3, $[N/(5^{NL-1})] = [121/25] = 4.84$ and integer remainder equal to 0.84. The reference number of the parent element is then $0.84 \times 5^2 = 21$, corresponding to Figure 2.

2.2. *Methodology*

The tri-tree grid generation process consists of the following steps:

(i) Define an initial equilateral triangle, within which the desired fluid domain will lie.
(ii) Define a set of seeding points about which the grid will be generated.
For example, Figure 4 shows an example of a circular cylinder in a unit square domain, although the scheme can be applied to other shapes. The grid generation starts from an equilateral triangle, which encloses the fluid domain, based on that a set of seeding points is properly distributed over its boundary.
(iii) If the triangle contains a seeding point, divide the triangle otherwise move to next one.
(iv) Repeat until the maximum division level has been reached.
Examples are given in Figures 5 and 6, which show the grid after one and nine successive divisions respectively.
(v) Subdivide all grid elements to minimum level.
Figure 7 shows the grid after division of all triangles to a minimum of level five. This process also involves removing from the grid any triangles that lie wholly outside the external flow boundary.
(vi) Apply face regulation (see Figure 8).
This involves performing further divisions to restrict the ratio of triangle sides sharing a common edge to 2:1 within the domain.

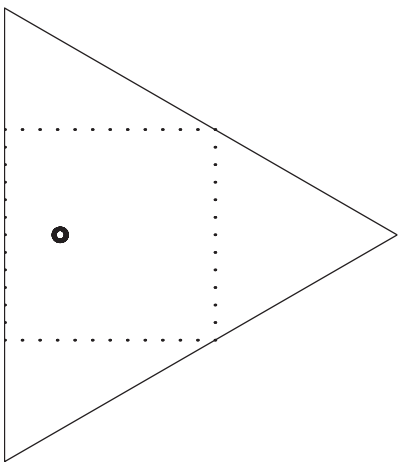

Figure 4. Seeding points.

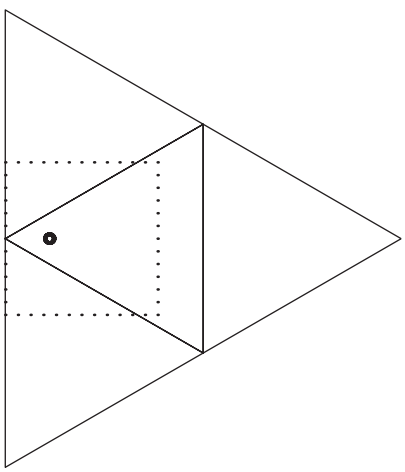

Figure 5. First division.

(vii) Eliminate hanging nodes.
Hanging nodes are vertices that lie at the centre of the face of an adjacent and larger element. They complicate the discretization equation because it is difficult to conserve flux numerically across hanging nodes. Connecting them to the third vertex of the adjacent larger triangle eliminates the hanging nodes as shown in Figure 9. This process creates two right-angled triangles from one equilateral triangle and the resulting grid then contains both equilateral and right-angled triangles.

(viii) Apply special boundary treatment around interior boundaries (see Section 2.3).

(ix) Apply corner regulation (see Figure 10).
This process smooths the transition between triangles of different size and involves performing further division of triangles that are connected at a vertex to a triangle

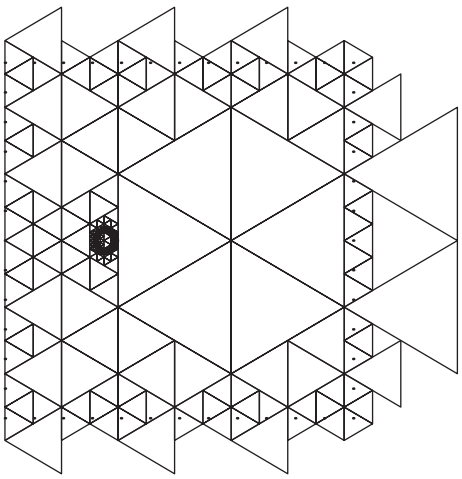

Figure 6. Ninth division.

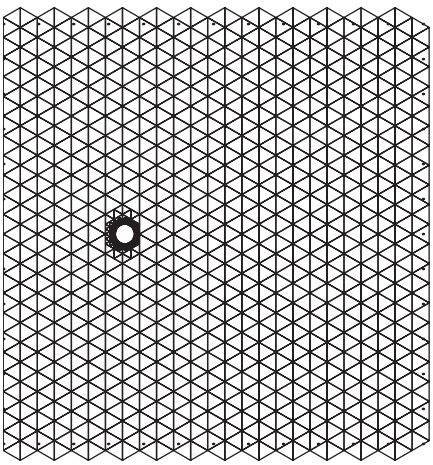

Figure 7. Application of minimum level 5.

of more than one division level difference. Thus, the side length ratio of triangles connected by a vertex is limited to a maximum of 2:1.

(x) Reorder cell and node numbers and store grid information.

After above procedures, the completed tri-tree grid is shown in Figure 11, which has a maximum division level of 9 and minimum division level of 5. In this grid, the size of the faces of the finest tri-tree elements is $1/2^8$ (maximum division level $=9$) times the length of the face of the initial triangle. The general formula for this length is

$$d = \frac{D}{2^n} \tag{3}$$

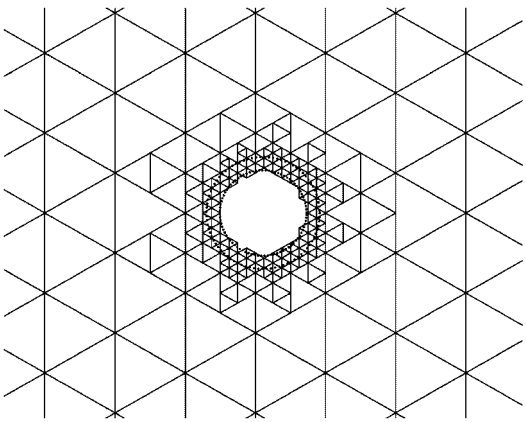

Figure 8. Grid after face regulation.

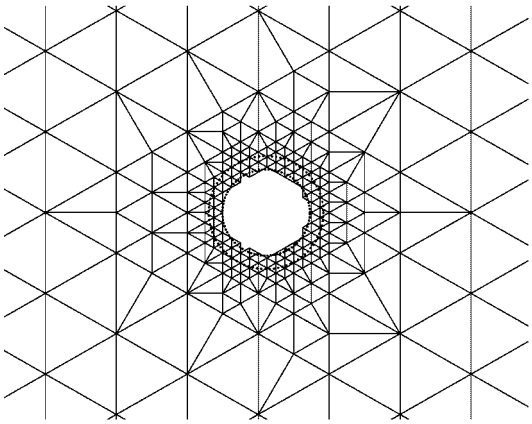

Figure 9. Elimination of hanging nodes.

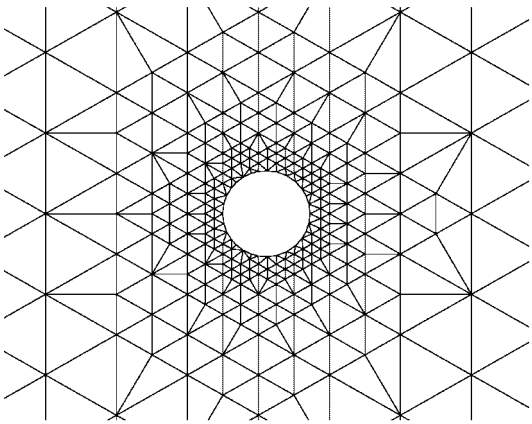

Figure 10. Grid after boundary treatment and corner regulation.

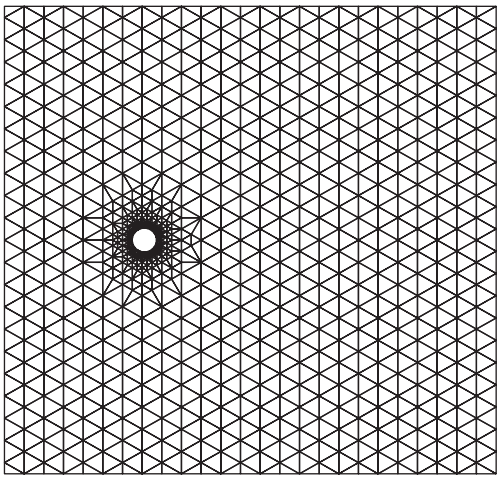

Figure 11. Entire grid, level 9.

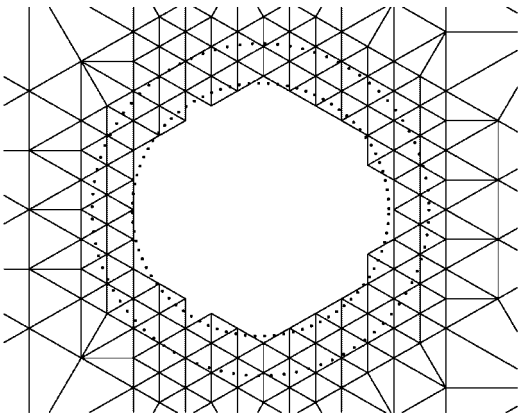

Figure 12. The vicinity of the cylinder.

where d is the size of the face of the finest element, D is the length of the face of the initial triangle and n is the level of the maximum division.

2.3. *Boundary treatment*

After the process of eliminating hanging nodes described at stage 7 in the last Section, the resulting elements in the vicinity of the cylinder are given in Figure 12, which shows that some of the nodes are inside the cylinder. A special treatment around the cylinder boundary is used to obtain a smooth approximation. Two steps are taken, as follows:

2.3.1. The stretching technique. First, the boundary nodes that lie close to the cylinder are selected and lines are extended from each of these nodes to the centre of the circular cylinder.

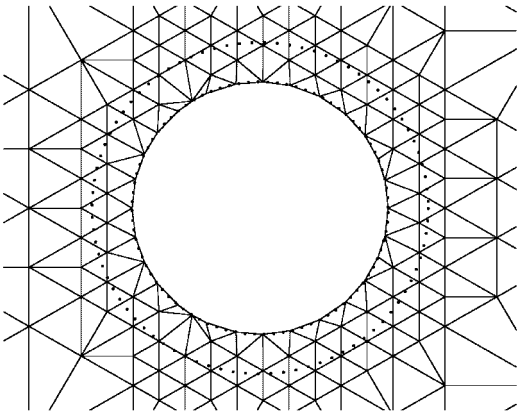

Figure 13. The stretching technique.

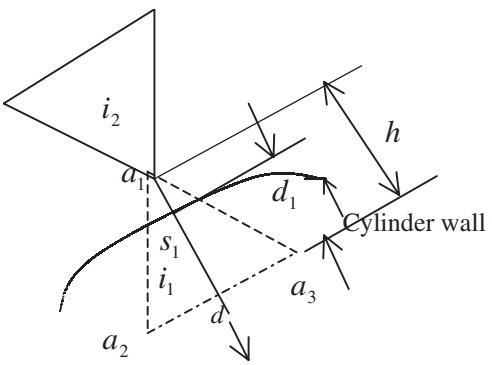

Figure 14. The cell i_1 is deleted.

The intersection between the line and the cylinder circumference will be the new node position as shown in Figure 13.

The key to the stretching technique is in making a decision on the critical distance normal to the actual cylinder wall. In other words, which elements close to the cylinder wall should be deleted or retained. Figure 14 shows a point s_1 lying on the cylinder circumference and located inside element i_1, which has two nodes inside the cylinder (a_2 and a_3) and the other a_1 in the opposite direction at distance a_1s_1 from the wall. An optimum ratio r is used to decide whether element i_1 is deleted or retained, which is defined as

$$r = \frac{d_1}{h} \tag{4}$$

where d_1 and h are the distances from s_1 and a_1 to the face a_2a_3 respectively.

If the ratio value r is larger than an optimum value, r_o, element i_1 is deleted as shown in Figure 15; a_1 is then stretched to s_1 so element i_2 is distorted. If r is less than r_o, the element

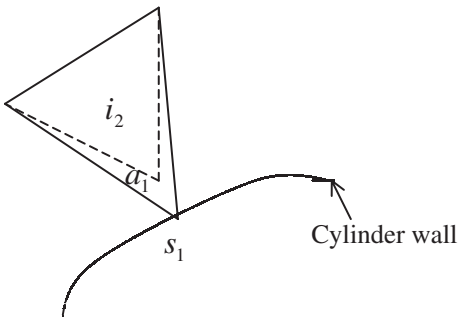

Figure 15. The cell i_2 is distorted.

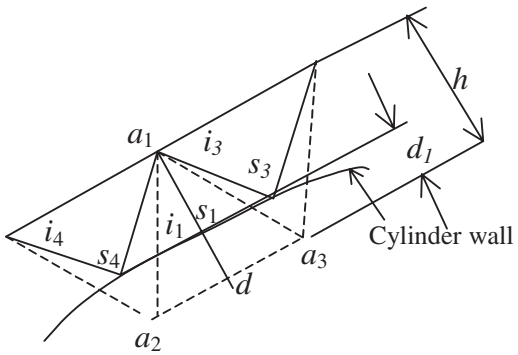

Figure 16. The cell i_1 is retained and i_1, i_3, and i_4 are distorted.

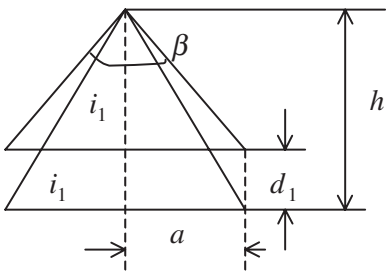

Figure 17. Notation associated with the optimum ratio.

i_1 is retained as shown in Figure 16; a_2 and a_3 are stretched to s_2 and s_3 so that elements i_1, i_3 and i_4 are distorted.

To determine r_o, we consider Figure 17 which shows triangle i_1 before and after distortion. Since i_1 is equilateral prior to distortion, we have

$$a/h = 1/\sqrt{3} \tag{5}$$

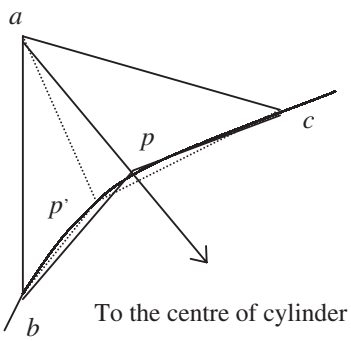

Figure 18. Elimination of obtuse angle.

In order to avoid obtuse angles that impair the quality of the solution, angle β should not exceed 90°. This implies that

$$\frac{a}{h-d_1} < \tan 45^\circ \Rightarrow a < h - d_1 \tag{6}$$

Introducing Equation (6) into Equation (5) yields,

$$\frac{h}{\sqrt{3}} > h - d_1 \Rightarrow d_1 < 0.423h \tag{7}$$

Hence, $r_o = 0.423$ will be the deciding value: if $d_1/h > 0.423$ the triangle is deleted, otherwise, it is retained and subsequently stretched.

2.3.2. Elimination of obtuse angles. The stretching technique ensures that no obtuse angles appear within the stretched triangle. However, this technique does not guarantee that obtuse angles will not arise in its neighbouring elements. This is especially true when two nodes on opposite sides of the cylinder boundary are stretched to their new positions. In this scenario, the combination of successive element distortions may create an obtuse angle within the neighbouring element. Obtuse angles within the grid may cause the accuracy of the numerical simulation to suffer, and so it is necessary to transform these angles into acute or right angles.

The correction procedure is implemented by firstly identifying these large angle cells such as abp' in Figure 18, where nodes b and p' lie on the cylinder surface. Lines are then defined from nodes that are outside the cylinder (e.g. node a) to the centre of the cylinder. The intersection between the line and the cylinder circumference will be the new node p. This creates two well-formed triangles abp and apc in this instance. Figure 19 shows the final result after the boundary treatment is applied to the cylinder boundary.

This boundary treatment has been developed for the circular cylinder considered here, but the technique may be adapted to an arbitrary boundary, when the line linking a grid node to the centre of the cylinder is replaced by a line normal to the surface.

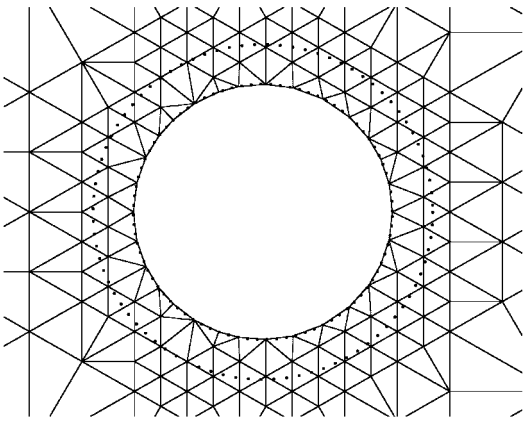

Figure 19. Elimination of obtuse angles.

2.4. Grid information storage and retrieval

When a triangular element is divided to produce four new elements, the parent number is deleted when the children are generated. During each generation procedure, the number of newly generated elements is added to the record of existing elements.

Two nodal numbering systems have to be used for each triangle: local and global nodal numbering. The local node numbers of a cell range from 1 to 3 in the anti-clockwise direction. The global node number is increased when a new node is generated in the refinement process. The co-ordinates of the nodes, the local and global node numbering, the boundary indicator information and cell reference numbers are all stored. Other information stored includes the starting and ending points for each face and the neighbours of each element. The tree structure so defined is sufficient to completely specify the element generation history for the purpose of adaptation.

3. TRI-TREE GRID ADAPTATION

The tri-tree described above has a naturally hierarchical data structure. It contains all flow and connectivity information sufficient to adapt the grid by a local grid refinement or derefinement process. The grid adaptation strategy assumes that there exists a good quality initial grid of the computational domain, which is taken to be the invariant base grid. The refinement process involves adding nodes to this base grid by face and element subdivision. Each change in the computational grid is tracked and recorded within the hierarchical data structure. The derefinement process is the inverse of refinement, where nodes, faces and elements are removed from the grid.

The process of grid adaptation is invoked automatically in response to flow solution criteria. It is desirable that refined regions correspond to regions of significant flow activity requiring increased resolution. Conversely, derefinement is applied in regions of insignificant flow activity where reduced resolution is desired for the sake of CPU efficiency. These criteria have important consequences for the overall operation of the adaptive solver.

Here the adaptation of the grid is based on a vorticity parameter. Before the grid may be adapted, it is necessary to calculate the vorticity value of each element defined as,

$$\omega = \left| \left(\frac{\mathrm{d}u}{\mathrm{d}y} \right) - \left(\frac{\mathrm{d}v}{\mathrm{d}x} \right) \right|$$

where u and v are velocity components in x and y directions respectively. The maximum vorticity $\omega_{\max}$ and the minimum vorticity $\omega_{\min}$ values are specified before the simulation starts and the grid is adapted regularly throughout the simulation at a prescribed number of time steps. If the vorticity of a given cell is greater than the prescribed maximum, $\omega_{\max}$, then that cell must be divided. There are two types of subdivision as there are two types of triangle. One is subdivision of equilateral triangles, which is regular division similar to the base grid subdivision. The other is the subdivision of right angle triangles, which is performed by firstly replacing the two right angle triangles with their equilateral parent element, and then subdividing the parent element into four equilateral triangles. If the vorticity of a given cell and all its siblings is less than the prescribed minimum, $\omega_{\min}$, and the cell is not a member of the base mesh, then its parent element is placed on the list of elements and the children are deleted.

It should be noted that the refinement and derefinement process does not change the value of the vorticity at a given point. It is therefore necessary to define a maximum and a minimum division level. When the refinement and derefinement process have gone beyond these levels, they will stop and the calculation will continue. This procedure is found to give satisfactory results at low Reynolds number provided in this paper.

Once the remeshing process is complete, face regulation, elimination of hanging nodes and corner regulations are performed. The grid is then reordered, nodes are numbered and the pointer system updated. All these procedures are the same as those described previously for the base grid generation.

4. THE FINITE VOLUME METHOD

4.1. Transport equation

Let ϕ represent a general variable, such as velocity. The general transport equation for ϕ can be written as

$$\frac{\partial(\rho\phi)}{\partial t} + \nabla \cdot (\rho \mathbf{U}\phi) = \nabla \cdot (\mu_\phi \nabla\phi) + \bar{s}^\phi \tag{8}$$

where $\bar{s}^\phi$ denotes a source, $\mathbf{U} = (u, v)$ is the velocity vector, ρ is the density of the fluid and μ_ϕ is the dynamic viscosity of the fluid. For the steady case, the first term is zero. If a flux vector $\mathbf{J}$ containing convection and diffusion is defined as

$$\mathbf{J} = \rho \mathbf{U}\phi - \mu_\phi \nabla\phi \tag{9}$$

then in steady state vector notation the transport equation reads

$$\nabla \cdot \mathbf{J} = \bar{s}^\phi$$

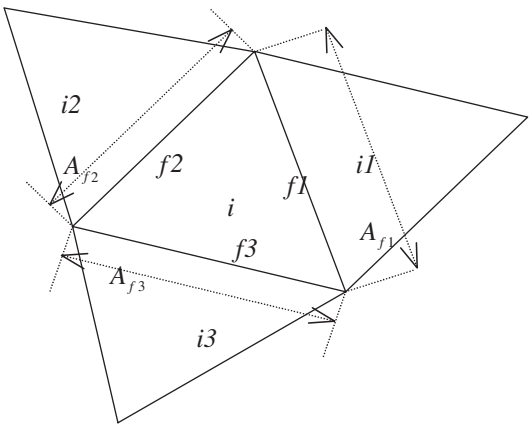

Figure 20. A triangular element i with its three neighbours $i1, i2, i3$.

Integrating this equation over a control volume (V_i bounded by surface A) and using the Gauss law of divergence give

$$\int_A \mathbf{J} \cdot \mathrm{d}\mathbf{A} = \int_{V_i} \bar{s}^{\phi} \, \mathrm{d}V \tag{10}$$

which, in the discretized form becomes

$$\sum_{fj=1}^{nf} (\mathbf{J} \cdot \mathbf{A})_{fj} = S^{\phi} \tag{11}$$

where nf is the total number of faces of a cell and is three for a triangular grid used in this paper and S^{ϕ} is the total source in the control volume. The left-hand side of Equation (10) has two parts: the net convective flux and the net diffusive flux, which will be discussed separately.

The convective flux contains the mass flux $m_{ff} = \rho A_{ff} U^{fj}$ multiplied by the scalar property ϕ. The face areas A_{fj} of element i are shown in Figure 20. The face normal velocities U^{fj} are calculated by:

$$U^{fj} = u_{fj} \cdot n_{xfj} + v_{fj} \cdot n_{yfj} \tag{12}$$

where $\mathbf{n}_{fj} = (n_{xfj}, n_{yfj})$ is the unit outward-pointing normal vector of the face, as shown in Figure 21.

The face velocities u_{fj} and v_{fj} may be calculated from their value at the cell centres where variables are defined. A three-point upstream-weighted quadratic interpolation (QUICK) scheme is used based on the notations in Figure 22. We have

$$\phi_{f1} = E_{fj}\phi_{i1} + G_{fj}\phi_i - I_{fj}\phi_{s1} \tag{13}$$

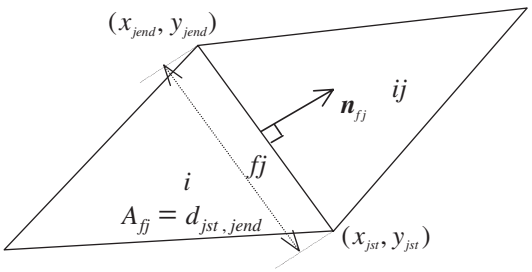

Figure 21. Notation associated with face fj.

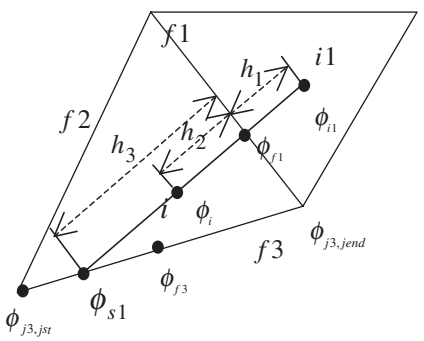

Figure 22. Notation associated with a face value when using the QUICK scheme.

where

$$E_{fj} = \left[\frac{h_2 h_3}{(h_1 + h_2)(h_1 + h_3)}\right], \quad G_{fj} = \left[\frac{h_1 h_3}{(h_1 + h_2)(h_3 - h_2)}\right], \quad I_{fj} = \left[\frac{h_1 h_2}{(h_1 + h_3)(h_3 - h_2)}\right] \tag{14}$$

ϕ_{s1} in Equation (13) is found through $\phi_{j3,jst}$ and $\phi_{f3}, \phi_{j3,jst}$ can be obtained through the values at the centres of the surrounding elements.

The second part of the flux vector **J** in Equation (9) represents diffusion. Across a given face fj, this becomes

$$-\{\mu_\phi \mathbf{A} \cdot \nabla\phi\}_{fj} = -\left\{\mu_\phi A_{fj}\left(n_x \frac{\partial\phi}{\partial x} + n_y \frac{\partial\phi}{\partial y}\right)_{fj}\right\} \tag{15}$$

We must now evaluate the derivatives at the faces. This is achieved by applying Green's formula to the control volume enclosed by the surface $a-b-c-d$ (see Figure 23) surrounding the midpoint of the face, i.e.

$$\left(\frac{\partial\phi}{\partial x}\right)_{fj} = \frac{1}{V_{fj}} \int \phi n_x \, \mathrm{d}A \qquad \left(\frac{\partial\phi}{\partial y}\right)_{fj} = \frac{1}{V_{fj}} \int \phi n_y \, \mathrm{d}A \tag{16}$$

where the integration is over the surface $a - b - c - d$ and V_{fj} is the enclosed volume. If bc and da are chosen to be parallel to the face, and ab and cd parallel to the line linking i

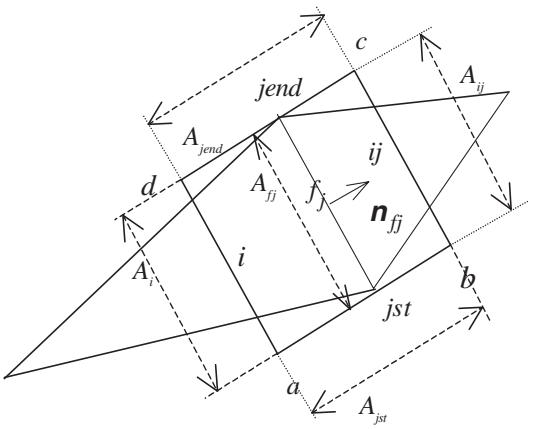

Figure 23. Notation associated with Equation (16).

and ij, we have

$$-\{\mu_\phi \mathbf{A}\cdot\nabla\phi\}_{fj} = -\frac{\mu_\phi A_{fj}}{V_{fj}}[A_{fj}(\phi_{ij}-\phi_i) + A_{j\text{end}}(n_{xfj}n_{xj\text{end}} + n_{yfj}n_{yj\text{end}})(\phi_{j\text{end}}-\phi_{jst})] \tag{17}$$

where ($n_{xj\text{end}}, n_{yj\text{end}}$ and $A_{j\text{end}}$ are normal vector and area of cd respectively. The first term on the right-hand side will be treated implicitly and the second term, which is due to the non-orthogonality between ab and bc, will be treated explicitly using values at the previous iteration.

Combining the expressions for convection and diffusion for a triangular cell gives

$$\sum_{j=1}^{3}[m_{fj}\phi_{fj} - (\mu_\phi A\nabla\phi)_{fj}] = S^\psi \tag{18}$$

where

$$S^\psi = S^\phi + \frac{\mu_\phi A_{fj}}{V_{fj}}A_{j\text{end}}(n_{xfj}n_{xj\text{end}} + n_{yfj}n_{yj\text{end}})(\phi_{j\text{end}}-\phi_{jst})$$

The resulting discretized equation is

$$a_p\phi_i = a_{f1}\phi_{il} + a_{f2}\phi_{i2} + a_{f3}\phi_{i3} + S^\psi + \sum_{j=1}^{3} I_{fj}m_{fj}\phi_{sfj} \tag{19}$$

where

$$a_{f1} = -E_{f1}m_{f1} + K_{f1}$$

$$a_{f2} = -E_{f2}m_{f2} + K_{f2}$$

$$a_{f3} = -E_{f3}m_{f3} + K_{f3}$$

$$a_p = (G_{f1}m_{f1} + K_{f1}) + (G_{f2}m_{f2} + K_{f2}) + (G_{f3}m_{f3} + K_{f3})$$

$$K_{fj} = \mu_\phi \frac{A_{fj}^2}{V_{fj}}$$

and E_{fj}, G_{fj}, I_{fj} are coefficients defined in Equation (14).

4.2. The pressure correction equation

Once ϕ in Equation (9) is taken as u or v, and $\bar{s}^\phi$ in Equation (10) is taken as $[(\partial p)/(\partial x)]$ or $[(\partial p)/(\partial y)]$, where p is the pressure, the result becomes the momentum equation for fluid flow. For a given pressure distribution, p^*, the above procedure gives a velocity field (u^*, v^*). In general, this velocity field does not satisfy the following continuity equation,

$$\frac{\partial}{\partial x}(\rho u) + \frac{\partial}{\partial y}(\rho v) = 0$$

which by integrating over an element, can be written in the discrete form

$$\sum_{j=1}^{3} m_{fj} = \sum_{j=1}^{3} \rho U^{fj} A_{fj} = 0 \tag{20}$$

In order to satisfy Equation (20), a pressure correction has to be introduced based on the SIMPLE algorithm. The new velocity field after pressure correction can be written as

$$u_i = u_i^* - \frac{V_i}{a_p}\left(\frac{\partial p'}{\partial x}\right)_i \quad \text{and} \quad v_i = v_i^* - \frac{V_i}{a_p}\left(\frac{\partial p'}{\partial y}\right)_i$$

We notice that above equation is defined at the centre of each cell. Interpolation is needed when it is substituted into Equation (20). We have

$$a_i p_i' = a_{pf1} p_{i1}' + a_{pf2} p_{i2}' + a_{pf3} p_{i3}' + S_p \tag{21}$$

where

$$a_{pf1} = \rho A_{f1}^2 W_{f1} \frac{1}{V_{f1}}$$

$$a_{pf2} = \rho A_{f2}^2 W_{f2} \frac{1}{V_{f2}}$$

$$a_{pf3} = \rho A_{f3}^2 W_{f3} \frac{1}{V_{f3}}$$

$$a_i = a_{pf1} + a_{pf2} + a_{pf3}$$

$$W_{fj} = \lambda_j \frac{V_i}{a_p} + (1 - \lambda_j)\frac{V_{ij}}{(a_p)_{ij}}$$

$$S_p = -\sum_{fj=1}^{nf} m_{fj}^* + \sum_{j=1}^{nf} \rho A_{fj} W_{fj} \frac{1}{V_{fj}} A_{j\text{end}}(n_{xfj} n_{xi\text{end}} + n_{yfj} n_{yj\text{end}})(p'_{j\text{end}} - p'_{jst})$$

Here λ_j is a weight function to interpolate the values at the cell centres to the intersection point of the two centres and the joint face of the two elements. After Equation (21) is solved, the pressure, velocities and mass flux are corrected as

$$p = p^* + \alpha_p p' \tag{22}$$

$$u_i = u_i^* - \frac{V_i}{a_p}\left(\frac{\partial p'}{\partial x}\right)_i \quad \text{and} \quad v_i = v_i^* - \frac{V_i}{a_p}\left(\frac{\partial p'}{\partial y}\right)_i \tag{23}$$

$$m_{fj} = m_{fj}^* - \rho A_{fj} W_{fj}\left(\frac{\partial p'}{\partial n}\right)_{fj} \tag{24}$$

where α_p is pressure under-relaxation factor.

Collocated grid systems based on the SIMPLE algorithm described above often suffer from numerical oscillation in the pressure field. In order to prevent such oscillation, the following term

$$\left(\frac{\partial p}{\partial n}\right)_{fj} - \left[\lambda_j\left(\frac{\partial p}{\partial n}\right)_i + (1-\lambda_j)\left(\frac{\partial p}{\partial n}\right)_{ij}\right] \tag{25}$$

is added to the convection (normal) velocities, as used by Davidson [9]. As a result, S_p in Equation (21) is modified with

$$m_{fj}^* = (\rho A_{fj} U^{fj*}) - \rho A_{fj} W_{fj}\left\{\left(\frac{\partial p}{\partial n}\right)_{fj} - \left[\lambda_j\left(\frac{\partial p}{\partial n}\right)_i + (1-\lambda_j)\left(\frac{\partial p}{\partial n}\right)_{ij}\right]\right\} \tag{26}$$

The above solution algorithm can be summarized as follows:

(a) initial pressure and velocity fields are defined;
(b) the coefficients a_p and a_{fj} in Equation (19) are calculated and the equation is solved using a point by point Gauss–Seidel solver;
(c) the coefficients for p' in Equation (21) are computed and the pressure-correction Equation is solved using a point by point Gauss–Seidel solver;
(d) the pressure, velocities and mass flux are corrected using Equations (22), (23) and (24) respectively;
(e) steps (a)–(d) are repeated until convergence is achieved, based on the assumption that the mass residuals in all cells or the sum of normalized residuals have fallen below a prescribed value.

For the unsteady flow, the first term of Equation (8) represents the rate of change term and is not equal to zero. The fully implicit scheme used here is based on that described by Versteeg and Malalasekera [10]. The discretized equations are the same as Equation (19) for the steady problems apart from a minor change to the central coefficient a_p:

$$a_p\phi_i = a_{f1}\phi_{i1} + a_{f2}\phi_{i2} + a_{f3}\phi_{i3} + S^{\psi} + \sum_{j=1}^{3} I_{fj} m_{fj}\phi_{sfj} + a_p^0\phi_i^0$$

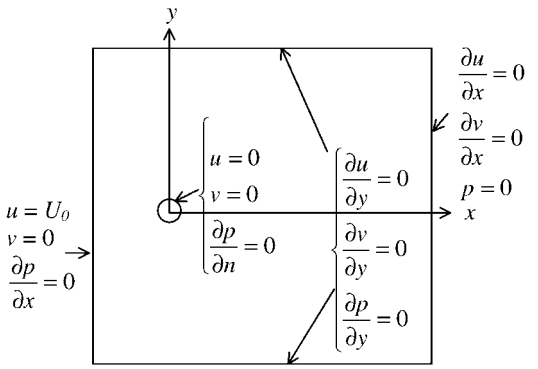

Figure 24. Boundary conditions.

where

$$a_p = (G_{f1}m_{f1} + K_{f1}) + (G_{f2}m_{f2} + K_{f2}) + (G_{f3}m_{f3} + K_{f3}) + a_p^0 \tag{27}$$

and

$$a_p^0 = \rho V_i / \Delta t$$

Here Δt is the time step and ϕ_i^0 indicates the variable at the previous time step. The rest of the coefficients are the same as those of Equation (19).

5. RESULTS

Results are presented here for simulations of low Reynolds number fluid flow past a single and multiple cylinders using the finite volume method with the adaptive tri-tree grids.

5.1. Initial values and boundary conditions

The inlet velocity U_0 is constant and the Reynolds number is defined by $Re = U_0 \times d_c/v$. Here, v is the kinematic viscosity of the fluid and d_c is the diameter of the cylinder. Initial values of the velocities, u, v, and the pressure, p, are set to zero everywhere apart from on the outer boundary, where the flow has an impulsive start.

No-slip conditions are imposed on the cylinder surface. The Dirichlet boundary condition is set for velocity at the inlet and pressure at the outlet. Elsewhere, the Neumann boundary condition is imposed, as illustrated in Figure 24. The calculation is considered to have converged when the sum of normalized residuals falls below 1.0×10^{-4}.

The computational configuration for flow past a circular cylinder which is used for the cases at $Re = 2.04$, $Re = 10$ and 40 considered below is shown in Figure 25. The centre of the cylinder is located a distance equal to $5d_c$ downstream from the inlet and $15d_c$ upstream from the outlet. The upper and lower lateral open boundaries of the domain are each $10d_c$ away from the centre of the cylinder. Some geometrical parameters of the closed wake defined in Figure 26 will be calculated.

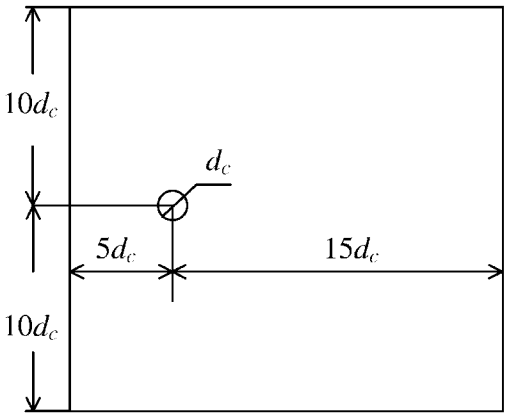

Figure 25. Computational configuration.

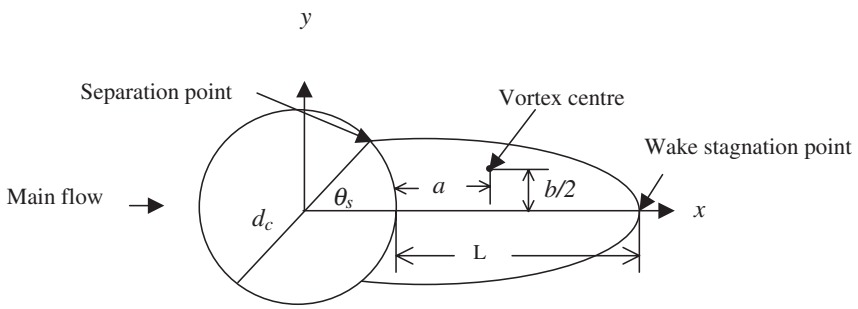

Figure 26. Geometrical parameters of the closed wake.

5.2. *Grid convergence test at* $Re = 2.04$

The lower limit for separation of the boundary layer is reported as $Re = 3.2$ by Nisi and Porter [11], $Re = 6.0$ by Homann [12] and $Re = 7$ by Dennis and Chang [13] for flow past a circular cylinder. For grid convergence tests, it is sensible to choose a case where the boundary layer remains attached or the vorticity in an element is less than the prescribed maximum and so does not require grid adaptation. Therefore, studies of the grid convergence on non-adaptive grids have been carried out for the case of $Re = 2.04$, which was investigated experimentally by Tritton [14].

The number of elements, nodes and the drag coefficient C_D (defined as 1 for the case of maximum level 10 and minimum level 6) are listed in Table I. It is clear that the solution is grid convergent and the grid used in case 3 is fine enough for this case. Figures 27 and 28 show the detail at the cylinder and the entire domain for the grid used in case 3. The converged solution shows good agreement with the experimental data published by Tritton [14].

Table I. Data for grid convergence test at $Re = 2.04$.

Case	Subdivision level		Cells	Nodes	Drag coefficient, C_D	
	Max	Min			Present study	Tritton [14]
1	10	6	1824	987	7.77	
2	11	6	2518	1363	7.33	
3	12	6	3957	2142	7.26	7.26
4	12	7	7061	3741	7.27	
5	13	6	8890	4726	7.25	

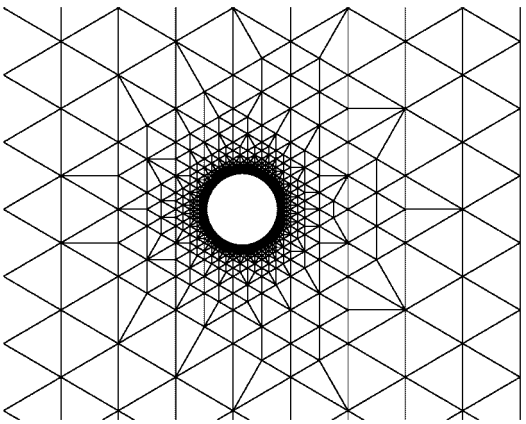

Figure 27. Grid detail near the cylinder.

5.3. *Simulation at* $Re = 10$

Steady flow simulation at Reynolds number, $Re = 10$, past a circular cylinder with adaptive grids is presented here. In this case, flow separation behind the cylinder forms two symmetric vortices.

The base grid is shown in Figure 28, and contains 3957 grids and 2142 nodes. The adapted maximum division level of 11 and the adapted minimum level of 6 are specified before the adaptation together with $\omega_{\max} = 3.0\ \mathrm{s}^{-1}$ and $\omega_{\min} = 0.1\ \mathrm{s}^{-1}$. After solver is run using the base grid, the adaptive routine and the solver are alternately and iteratively run until no more new elements are generated. The total number of iterations is 5 and the final adapted grid contains 4125 grids and 2226 nodes shown in Figure 29.

Figure 30 illustrates the velocity vectors in the vicinity of the cylinder. Figure 31 shows pressure contours at $\Delta p = 2.73 \times 10^{-1}$ Pa. These flow patterns are found to be in good agreement with those provided by Greaves [15] and Saalehi [16]. The drag coefficient is found to be $C_D = 2.99$, which is in reasonable agreement with that obtained numerically by Collins and Dennis [17], $C_D = 2.94$.

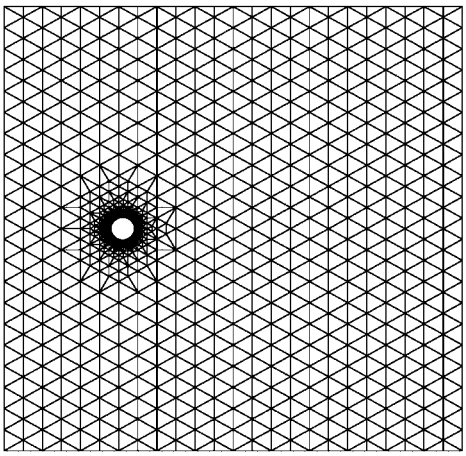

Figure 28. Entire grid.

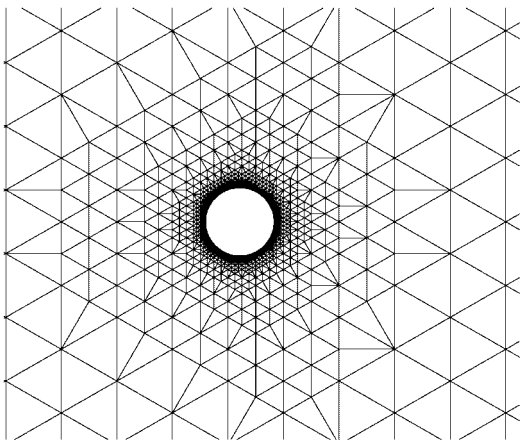

Figure 29. Detailed adapted grid near the cylinder at $Re = 10$.

5.4. Simulation at $Re = 40$

Although the flow past a circular cylinder for $Re = 40$ is steady, simulations were carried out using the unsteady formulation to validate the time-dependent finite volume method. The simulation used a non-dimensional time step $\Delta t^* = 1.0$, where $t^* = U_0 \times t/d_c$, and steady state is presumed to occur after the sum of normalized residuals falls below 1.0×10^{-4} for each successive time step. The simulation took 14 adaptations and stopped at non-dimensional time $t^* = 14$ at which point no more new elements or nodes were generated. The base grid is shown in Figure 28 and the fully adapted grid in Figure 32. Figure 33 illustrates the velocity vectors in vicinity of the cylinder and Figure 34 shows pressure contours at $\Delta p = 3.832$ Pa.

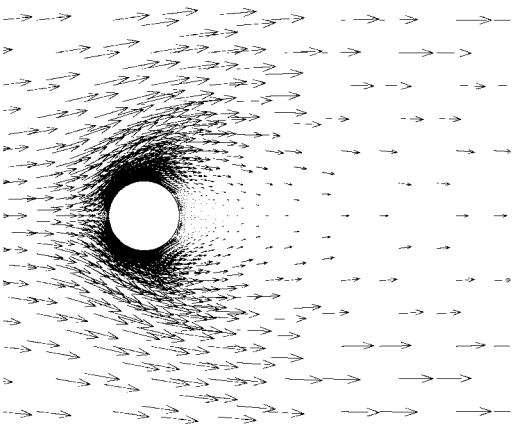

Figure 30. Velocity vectors at $Re = 10$.

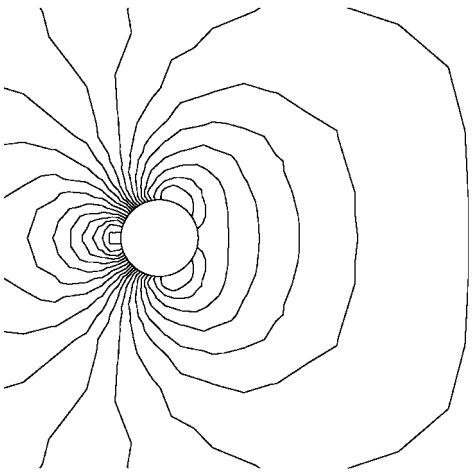

Figure 31. Pressure contours at $Re = 10$.

Figure 35 depicts the time history of the drag coefficient C_D and shows the time convergence of the method. The evolution in time of the: close-wake length parameter, L/d_c, is shown in Figure 36; position of the vortex centres (a/d_c and b/d_c) are presented in Figures 37 and 38; separation angle, θ_s, is shown in Figure 39. The time variation of each of these parameters shows good agreement between the present results and those of the experimental data given by Coutanceau and Bouard [18].

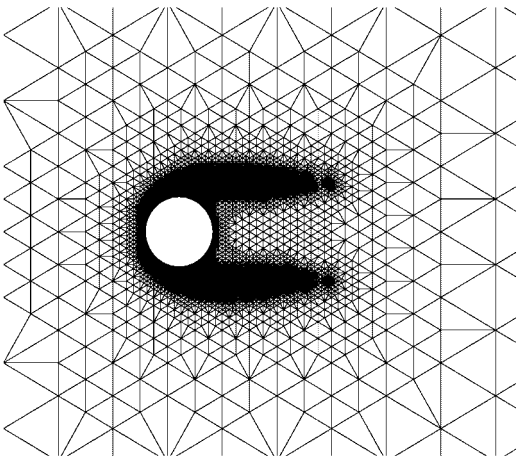

Figure 32. Detail of adapted grid at $Re=40$.

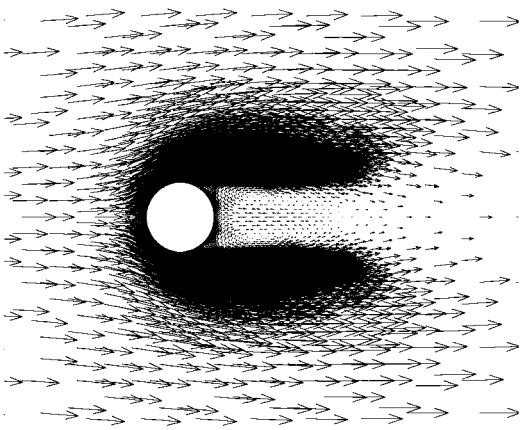

Figure 33. Velocity vectors at $Re=40$.

5.5. *Simulation at* $Re=200$

The flow past a cylinder at $Re=200$ has an unsteady wake formed by shed vortices. Figure 40 show the streamlines in sequence for one complete cycle of Kàmàn vortex shedding with $\Delta\psi=0.32\,\mathrm{m^2\,s^{-1}}$, where ψ is the stream function. These patterns are in good agreement with numerical simulations provided by Chen *et al.* [19].

Table II shows a comparison between the present results (C_D, C_L) and the Strouhal number, $S=f\times d_c/U_0$ where f is the vortex shedding frequency) and those obtained by experiment and other numerical simulations. The present numerical data are in reasonable agreement with the other published results.

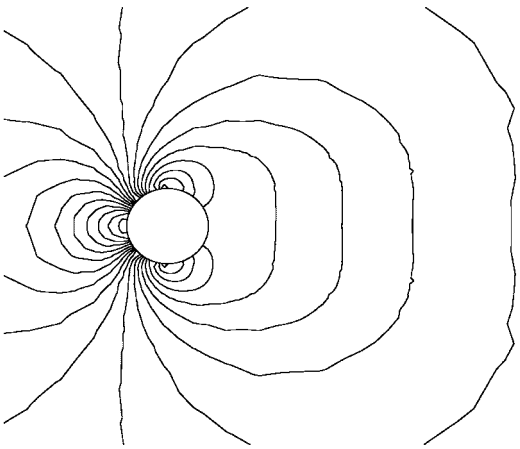

Figure 34. Pressure contours at $Re=40$.

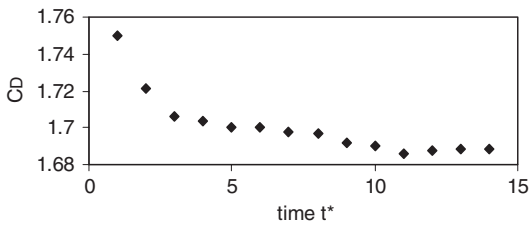

Figure 35. Time history of the drag coefficient.

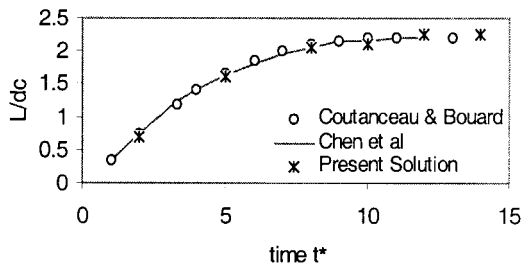

Figure 36. Evolution with time of L/d_c.

5.6. *Flow past multiple circular cylinders at* $Re=40$

Arrays of cylinders, which may be subject to flow interaction, occur in various industrial applications, such as pipe bundles, closely spaced tubular members of offshore jacket structures and heat exchanger tubes. In this section, interactions due to fluid flow past fixed multiple

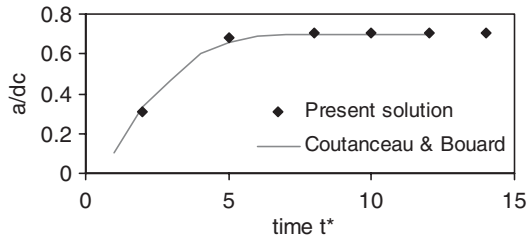

Figure 37. Evolution with time of a/d_c.

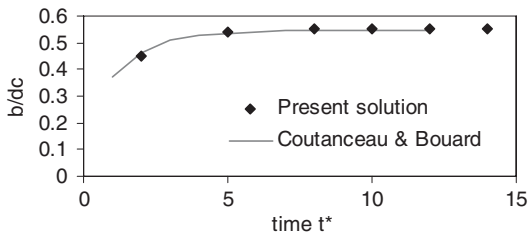

Figure 38. Evolution with time of b/d_c.

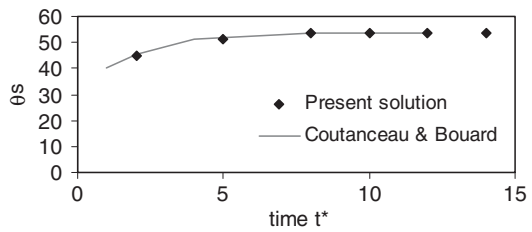

Figure 39. Evolution with time of the cylinder separation angle, θ_s.

circular cylinders at $Re=40$ are predicted. The flow interaction between two or three cylinders depends on the non-dimensional distance between the centres of the cylinders, denoted by T/d_c in the cross-flow direction and P/d_c in the flow direction as shown in Figures 41, 42 and 43.

The transverse arrangement will be considered first. The flow interaction between two cylinders depends on their spacing and has been calculated here for arrangements at $T/d_c=2.0$ and $T/d_c=5.0$. The diameter of the cylinder, d_c, is taken as 0.05 m (1/25 of the domain length). The final adapted grids for two circular cylinders placed in transverse arrangement at $T/d_c=2.0$ and $T/d_c=5.0$ are shown in Figures 44 and 45. Figures 46 and 47 illustrate the velocity vectors in the vicinity of the cylinders. Figures 48 and 49 show pressure contours at $\Delta p=5.13$ Pa and $\Delta p=4.63$ Pa respectively.

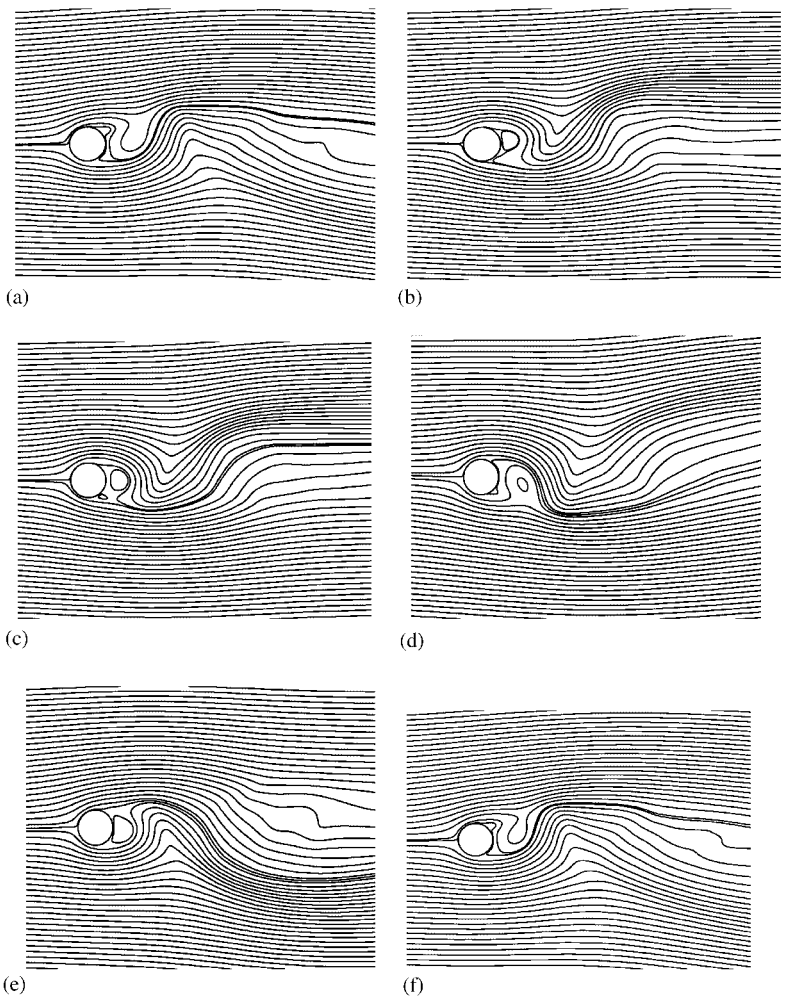

Figure 40. Streamline pattern sequence over one cycle of Kàmàn vortex shedding.

Table II. Drag, lift and Strouhal number at $Re = 200$.

	C_D		C_L		S
	Max.	Min.	Max.	Min.	
Present study	1.50	1.32	0.71	−0.59	0.200
Wille [20] (experimental)					
Roshko [21] (experimental)	1.3				0.19
Lecointe and Piquet [22]	1.50	1.42	0.70	−0.70	0.227
Chen *et al.* [19]	1.37	1.29	0.72	−0.72	0.197
Chan and Anastasion [8]	1.53	1.43	0.63	−0.63	0.183

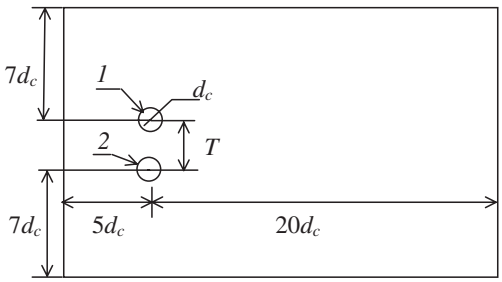

Figure 41. Computational configuration in transverse arrangement.

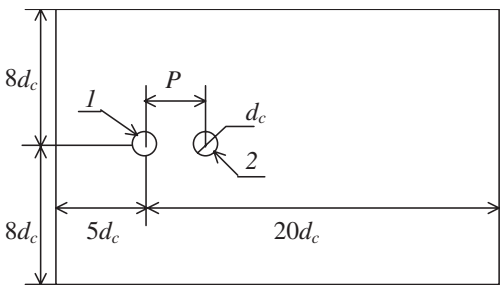

Figure 42. Computational configuration in tandem arrangement.

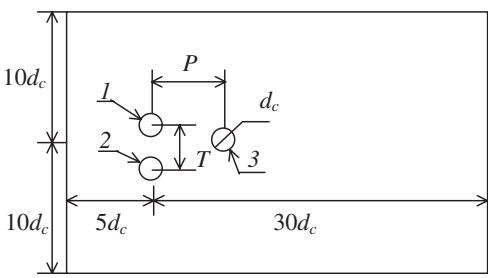

Figure 43. Computational configuration for three cylinders.

The cylinder spacing affects the flow patterns around the two cylinders. The flow patterns can be distinguished by examining the closed wake length L, the position of the vortex centres (a, b) and the separation angles, $\theta_{s.}$ These parameters are all listed in Table III. The drag and lift data are recorded in Table VI. The drag coefficients for both cylinders in both transverse arrangements are greater than that for the single cylinder.

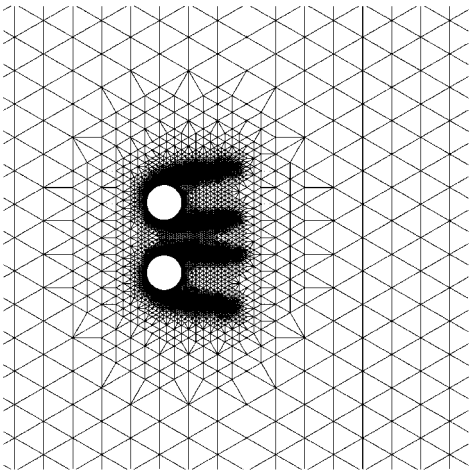

Figure 44. Adapted grid at $T/d_c = 2.0$.

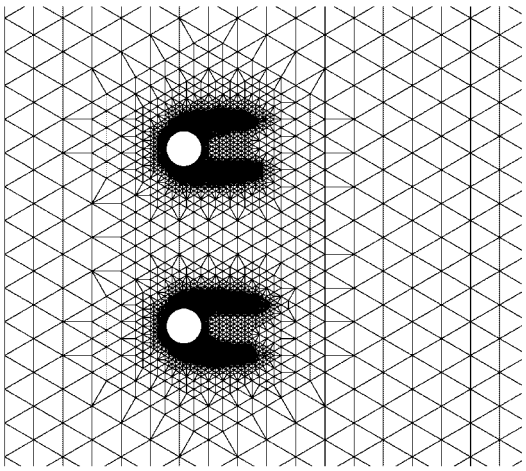

Figure 45. Adapted grid at $T/d_c = 5.0$.

Flow past two cylinders in tandem arrangement $P/d_c = 2.0$ and $P/d_c = 5.0$ is considered next. The final adapted grids for $P/d_c = 2.0$ and $P/d_c = 5.0$ are shown in Figures 50 and 51. Figures 52 and 53 illustrate the velocity vectors close to the cylinders. Figures 54 and 55 show pressure contours at $\Delta p = 3.42$ Pa and $\Delta p = 3.83$ Pa respectively.

Table IV summarizes the geometrical parameters of the closed wake for the two tandem arrangements considered and for the single cylinder. The drag and lift data are recorded in Table VI. These data show that the result of flow interference between two cylinders in tandem is that the drag coefficient for the upstream cylinder is slightly lower than for a single cylinder and for the downstream cylinder is much lower than for a single cylinder. The drag coefficient for the downstream cylinder for $P/d_c = 5.0$ has a higher value than for $P/d_c = 2.0$.

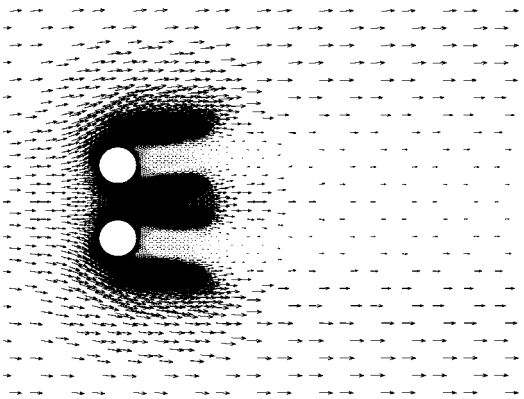

Figure 46. Velocity vectors at $T/d_c = 2.0$.

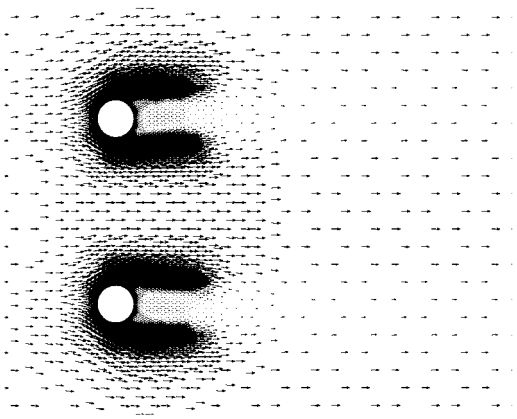

Figure 47. Velocity vectors at $T/d_c = 5.0$.

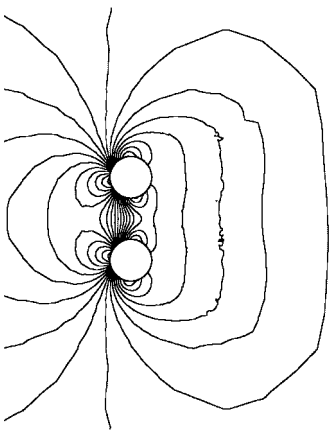

Figure 48. Pressure contours at $T/d_c = 2.0$.

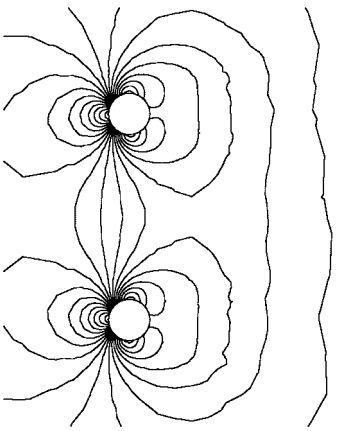

Figure 49. Pressure contours at $T/d_c = 5.0$.

Table III. Geometrical parameters of the closed wake: (a) definition; (b) predicted values.

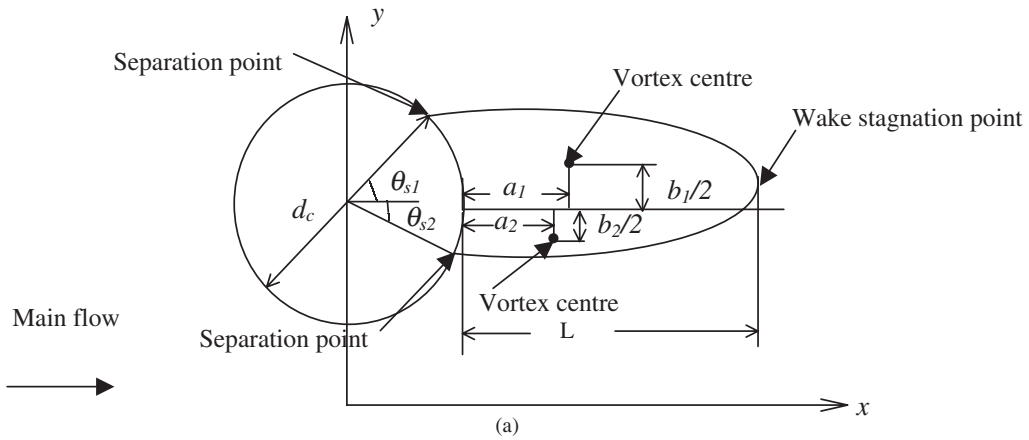

(a)

$Re = 40$	L/d_c	θ_{s1}	θ_{s2}	a_1/d_c	b_1/d_c	a_2/d_c	b_2/d_c
A single cylinder	2.26	53.56°	—	0.75	0.58	—	—
$T/d_c = 2.0$	2.0	55.88°	−43.24°	0.6	0.5	0.70	0.24
$T/d_c = 5.0$	2.20	52.43°	−48.92°	0.78	0.62	0.60	0.55

(b)

As may be expected, less interaction occurs for the $P/d_c = 5.0$ spacing and so the value of drag coefficient for the upstream cylinder in this case is more similar to the single cylinder than for the $P/d_c = 2.0$ case. However, with both cases, the force on the downstream cylinder is dramatically reduced by its presence in the wake of the upstream cylinder.

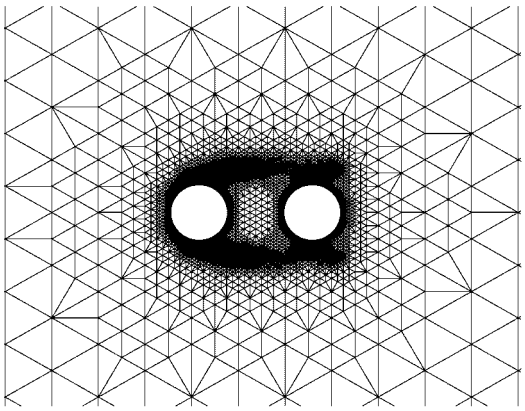

Figure 50. Adapted grid at $P/d_c = 2.0$.

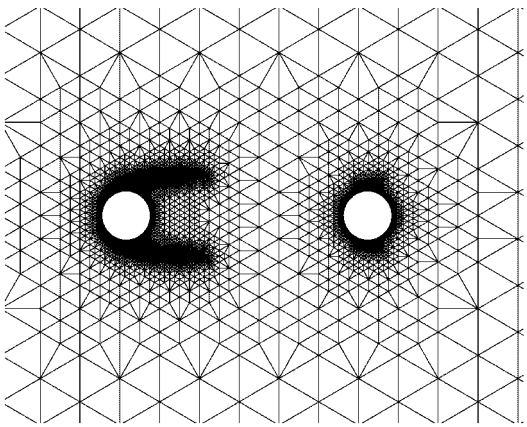

Figure 51. Adapted grid at $P/d_c = 5.0$.

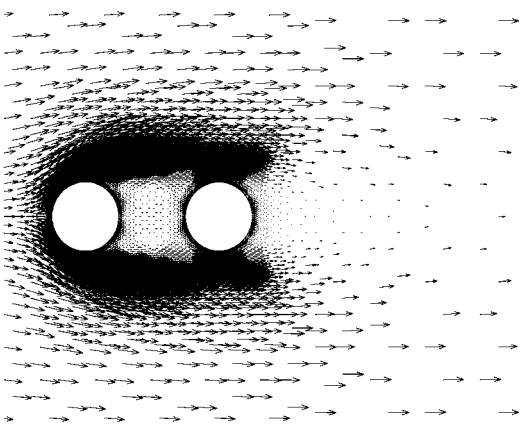

Figure 52. Velocity vectors at $P/d_c = 2.0$.

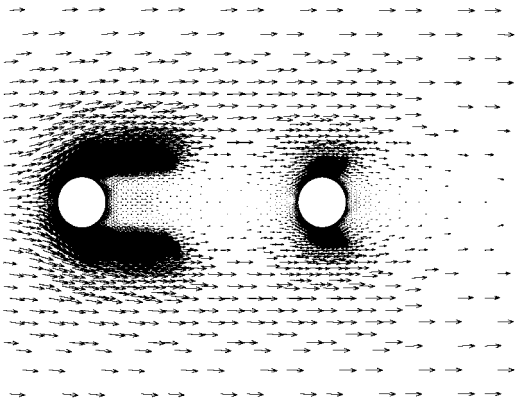

Figure 53. Velocity vectors at $P/d_c = 5.0$.

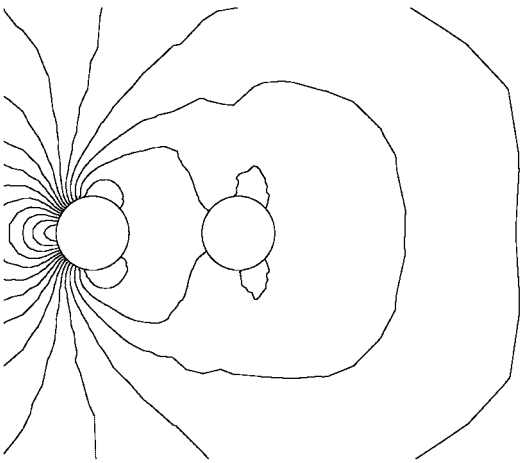

Figure 54. Pressure contours at $P/d_c = 2.0$.

5.7. *Flow past three cylinders*

The grid for three circular cylinders placed in arrangement at $T/d_c = 2.0$ and $P/d_c = 2.5$, in which the third cylinder is shielded from the incoming flow behind the pair of transverse cylinders, is shown in Figure 56. Figure 57 illustrates the velocity vectors close to the cylinder, Figure 58 shows pressure contours at $\Delta p = 5.01$ Pa. These flow patterns have been found in good agreement with numerical simulations by Greaves and Borthwick [23].

The closed wake length L, the position of the vortex centres (a, b) and the separation angles, θ_s are listed in Table V. The drag and lift coefficients are given in Table VI.

For this case, it can be seen that the flow interaction around the upstream cylinders behaves similarly to the transverse cylinders at $T/d_c = 2.0$. The force on each cylinder is larger than for

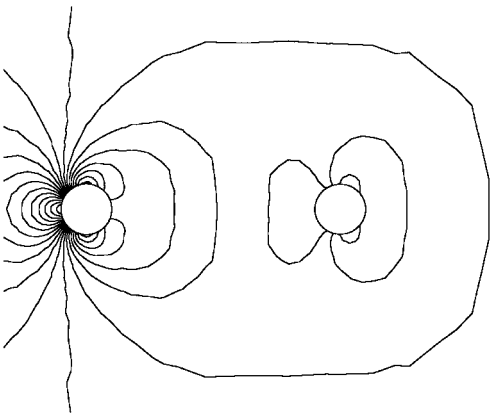

Figure 55. Pressure contours at $P/d_c = 5.0$.

Table IV. Geometrical parameters of the closed wake: (a) definition; (b) predicted values.

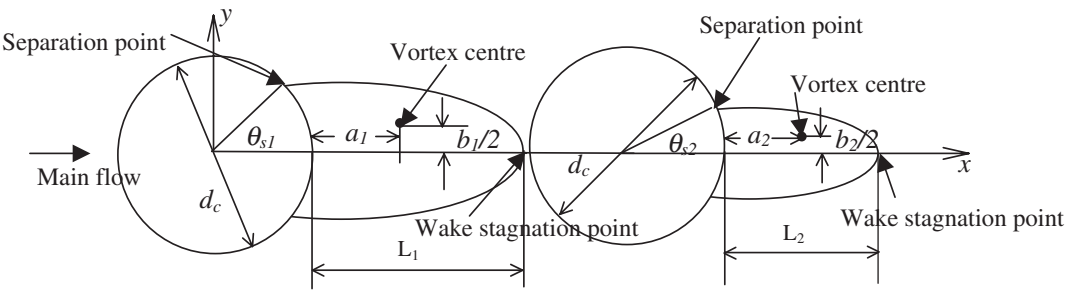

(a)

$Re = 40$	L_1/d_c	L_2/d_c	θ_{s1}	θ_{s2}	a_1/d_c	b_1/d_c	a_2/d_c	b_2/d_c
A single cylinder	2.26	—	53.56°	—	0.75	0.58	—	—
$P/d_c = 2.0$	—	1.74	54.32°	40.36°	0.5	0.65	0.7	0.48
$P/d_c = 5.0$	2.9	2.9	54.32°	40.74°	1.4	0.56	0.6	0.2

(b)

the single cylinder. However, the presence of the third cylinder reduces the force compared to that calculated for two cylinders alone. The table shows there is discrepancy between the results calculated here and those given by Greaves and Borthwick [23]. This is probably because the triangular elements used here provide a better approximation to a curved boundary than the square elements adopted by Greaves and Borthwick.

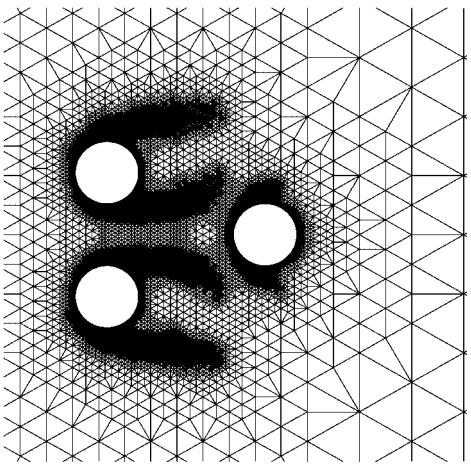

Figure 56. Detail of adapted grid.

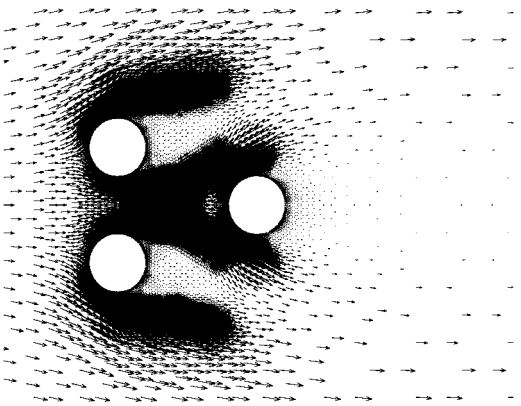

Figure 57. Velocity vectors.

6. CONCLUSION

The paper has presented the study of the adaptive tri-tree grid generation and the application of the finite volume method on the unstructured grid. The work has demonstrated that the tri-tree unstructured grid is more flexible and gives a smoother approximation to a curved boundary. It shows that the algorithm has potential to be used for complex geometry. The local refinement is particularly useful for accurate simulation of vortical structures in the flow. Investigation into the flow past single and multiple cylinders has demonstrated that the numerical results are in reasonable agreement with published data. Although the calculated examples are at low Reynolds number, the developed method can in principle be applied to flow at high Reynolds number as well.

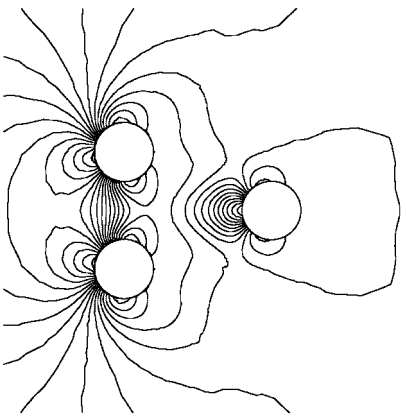

Figure 58. Pressure contours.

Table V. Geometrical parameters of the closed wake: (a) definition; (b) predicted values.

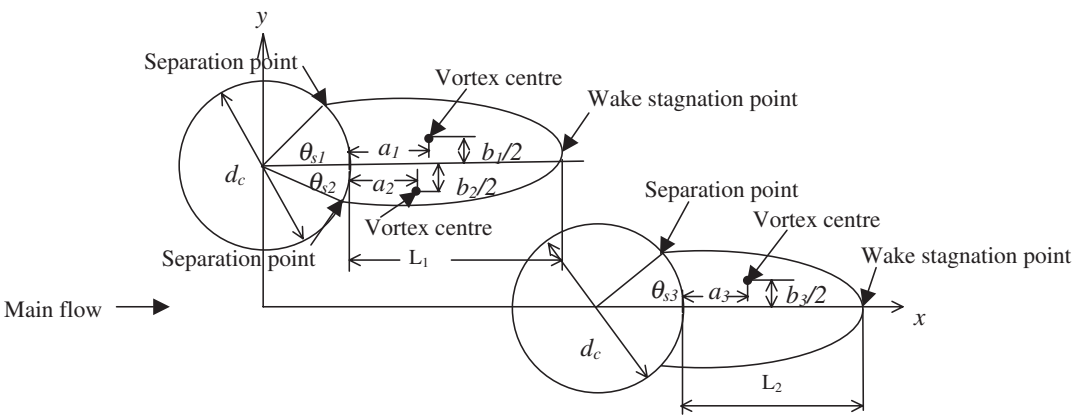

(a)

$Re=40$	L_1/d_c	L_2/d_c	θ_{s1}	θ_{s2}	θ_{s3}	a_1/d_c b_p/d_c	a_2/d_c b_2/d_c	a_3/d_c b_3/d_c
$T/d_c=2.0$						0.34	0.62	3.8
$P/d_c=2.5$	1.1	8.6	60.25°	−43.03°	72.08°	0.868	0.18	0.936

(b)

The studies suggest that the algorithm is a contender for many engineering applications. Although the selected cylinder configurations are special, they provide good examples of the strength of the present scheme. This analysis has laid the foundation for further investigation of more complex flow configurations and may also be extended to general three-dimensional simulations.

Table VI. The drag and lift coefficients for $Re=40$ flow past a single cylinder and multi-cylinders comparison with numerical data reported by [a]Dennis and Chang [13] and [b]Greaves and Borthwick [23].

$Re=40$	Drag coefficient, C_D						Lift coefficient, C_L					
	Present study			Published data			Present study			Published data		
	1	2	3	1	2	3	1	2	3	1	2	3
A single cylinder	1.69			1.62[a]			— 3.84 E-03					
Two cylinders $T/d_c=2.0$	2.18	2.18		1.77[b]	1.77[b]		0.63	— 0.68		0.37[b]	— 0.39[b]	
Two cylinders $T/d_c=5.0$	1.87	1.87					0.12	— 0.13				
Two cylinders $P/d_c=2.0$	1.63	0.15					— 6.50 E-03	— 4.37 E-03				
Two cylinders $P/d_c=5.0$	1.66	0.44					— 9.72 E-03	9.68 E-02				
Three cylinders $T/d_c=2.0$ $P/d_c=2.5$	2.03	2.04	0.93	1.63[b]	1.64[b]	0.71[b]	0.67	— 0.69	— 1.02 E-4	0.36[b]	— 0.38[b]	4.0 E-3[b]

REFERENCES

1. Wille SØ. A Structured tri-tree search method for generation of optimal unstructured finite element grids in two and three dimensions. *International Journal for Numerical Methods in Fluids* 1992; **14**:861–881.
2. Samet H. *The Design and Analysis of Spatial Data Structures*. Addison-Wesley, Reading, MA, 1990.
3. Samet H. *Applications of Spatial Data Structure*. Addison-Wesley, Reading, MA, 1990.
4. Patankar SV. *Numerical Heat Transfer and Fluid Flow*. Taylor and Francis, London, 1980.
5. Franke R, Rodi W, Schönung B. Numerical calculation of laminar vortex shedding flow past cylinders. *Journal of Wind Engineering and Industrial Aerodynamics* 1990; **35**:237–257.
6. Pan D, Cheng JC. A second-order upwind finite-volume method for the Euler solution on unstructured triangular methods. *International Journal for Numerical Methods in Fluids* 1993; **16**:1079–1098.
7. Thomadakis M, Leschziner M. A pressure-correction method for the solution of incompressible viscous flows on unstructured grids. *International Journal for Numerical Methods in Fluids* 1996; **22**:581–601.
8. Chan CT, Anastasion K. Solution of incompressible flows with or without a free surface using the finite volume method on unstructured triangular meshes. *International Journal for Numerical Methods in Fluids* 1999; **29**: 35–57.
9. Davidson L. A pressure correction method for unstructured meshes with arbitrary control volumes. *International Journal for Numerical Methods in Fluids* 1996; **22**:265–281.
10. Versteeg HK, Malalasekera W. *Computational Fluid Dynamics*: *The Finite Volume Method*. Longman Scientific & Technical Press, U.K., 1995.
11. Nisi H, Porter AW. On eddies in air. *Philosophical Magazine* 1923; **6**:754.
12. Homann F. *Zeitschrift fuer Angewandte Mathematical Mechanics* 1936; **6**:53.
13. Dennis SCR, Chang GZ. Numerical solution for steady flow past a circular cylinder at Reynolds numbers up to 100. *Journal of Fluid Mechanics* 1970; **42**:471–489.

14. Tritton DJ. Experiments on the flow past a circular cylinder at low Reynolds numbers. *Journal of Fluid Mechanics* 1959; **6**:547–561.
15. Greaves DM. Numerical modelling of laminar separated flow and inviscid steep waves using adaptive hierarchical meshes. *D.Phil. Thesis*, University of Oxford, 1995.
16. Saalehi A. Quadtree-based finite element modelling of laminar separated flow past a cylinder. *D.Phil. Thesis*, University of Oxford, 1995.
17. Collins WM, Dennis SCR. Flow past an impulsively started circular cylinder. *Journal of Fluid Mechanics* 1973; **60**:105–127.
18. Coutanceau M, Bouard R. Experimental determination of the main features of the viscous flow in the wake of a circular cylinder in uniform translation. Part 2. Unsteady flow. *Journal of Fluid Mechanics* 1977; **79**:257–272.
19. Chen YH, Yang SC, Yang JY. Implicit weighted essentially non-oscillatory schemes for the incompressible Navier–Stokes equations. *International Journal for Numerical Methods in Fluids* 1999; **31**:747–765.
20. Wille R. Kámán vortex streets. *Advances in Applied Mechanics* 1960; **6**:273–281.
21. Roshko A. On the development of turbulent wakes from vortex streets. *NACA Report*, 1954 p. 1191.
22. Lecointe Y, Piquet J. On the use of several compact methods for the study of unsteady incompressible viscous flow around a circular cylinder. *Computational Fluids* 1984; **12**:255–280.
23. Greaves DM, Borthwick AGL. Adaptive quadtree grids applied to the computation of flow past circular cylinders. *Proceedings of the Eighth International Conference on the Behaviour of Offshore Structures*, Delft, The Netherlands, 1997, pp. 11–23.

